Two-photon imaging of cerebral hemodynamics and neural activity in awake and anesthetized marmosets

Thom P. Santisakultarm[a], **Calvin J. Kersbergen**[a], **Daryl K. Bandy**[b], **David C. Ide**[c], **Sang-Ho Choi**[a], and **Afonso C. Silva**[a,*]

[a]Cerebral Microcirculation Section, Laboratory of Functional and Molecular Imaging, National Institute of Neurological Disorders and Stroke, National Institutes of Health, Bethesda, MD, 20892, USA

[b]Section on Instrumentation, National Institute of Neurological Disorders and Stroke, National Institutes of Health, Bethesda, MD, 20892, USA

[c]Section on Instrumentation, National Institute of Mental Health, National Institutes of Health, Bethesda, MD, 20892, USA

Abstract

Background—Marmosets are a powerful, emerging model for human behavior and neurological disorders. However, longitudinal imaging modalities that visualize both cellular structure and function within the cortex are not available in this animal model. Hence, we implemented an approach to quantify vascular topology, hemodynamics, and neural activity in awake marmosets using two-photon microscopy (2PM).

New method—Marmosets were acclimated to a custom stereotaxic system. AAV1-GCaMP5G was injected into somatosensory cortex to optically indicate neural activity, and a cranial chamber was implanted.

Results—Longitudinal 2PM revealed vasculature and neurons 500 μm below the cortical surface. Vascular response and neural activity during sensory stimulation were preserved over 5 and 3 months, respectively, before optical quality deteriorated. Vascular remodeling including increased tortuosity and branching was quantified. However, capillary connectivity from arterioles to venules remained unchanged. Further, behavioral assessment before and after surgery demonstrated no impact on cognitive and motor function. Immunohistochemistry confirmed minimal astrocyte activation with no focal damage. Over 6 months, total cortical depth visualized decreased. When under anesthesia, the most prominent isoflurane-induced vasodilation occurred in capillaries and smaller arterioles.

Comparison with existing method(s)—These results demonstrate the capability to repeatedly observe cortical physiology in awake marmosets over months.
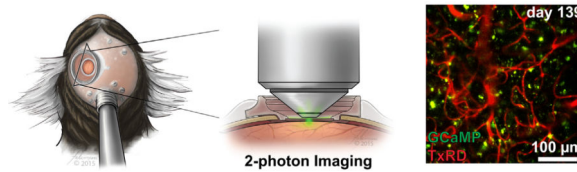
---

*Corresponding author. silvaa@ninds.nih.gov (A.C. Silva).

Conclusions—This work provides a novel and insightful technique to investigate critical mechanisms in neurological disorders in awake marmosets without introducing confounds from anesthesia.

GRAPHICAL ABSTRACT

Keywords

Non-human primates; Two-photon laser scanning microscopy; GCaMP; Neurovascular coupling; Vascular topology; Somatosensory activation

1. Introduction

Marmosets are a powerful, emerging model for human behavior and neurological diseases. Many disorders of higher brain function are difficult to closely model in rodents (Mansfield, 2003). In addition to having markedly different neuroanatomy, endocrinology, metabolism, and genetics, extrapolation of social and behavioral evaluation from rodents to primates can be uncertain or unavailable. Hence, the use of non-human primates in biomedical research can help neuroscientists address these concerns. Although many studies have used the rhesus macaque as a biomedical model, the common marmoset (*Calithrix jacchus*) is fast emerging as an attractive alternative. Similar to humans, marmosets have neural specializations such as face-selective areas in the visual cortex (Hung et al., 2015; Burman et al., 2015) and rich social interactions including biparental care of offspring. Compared to rhesus macaques, marmosets are smaller (350 g), reach sexual maturity faster (18 months), have a shorter gestational period (5 months), often give birth to fraternal twins or triplets, and produce up to 80 progeny during their life. A marmoset's short natural lifespan (12 years), compared to a macaque's (25 years), is also specifically beneficial for the study of age-related dysfunctions. For instance, aged marmosets (>7 years) display neurodegenerative changes, such as reduced neurogenesis and beta-amyloid deposition (Mansfield, 2003). Most importantly, marmosets are the first primates to have demonstrated germline transmission that allows for natural breeding of transgenic marmoset models of human neurological conditions, including Parkinson's disease, amyotrophic lateral sclerosis, and schizophrenia (Sasaki et al., 2009). Therefore, the use of marmosets in biomedical science has tremendous translational appeal for both basic and clinical research.

Understanding neural activity and cerebral blood flow regulation in the marmoset is an attractive step for deciphering the human brain and mechanisms of disease. Cerebral blood flow is controlled with exquisite precision to ensure that homeostasis of the delicate cellular environment is maintained at all times, including during neural activation when metabolic demand is elevated. Such relationship between neural activation and cerebral blood flow, termed neurovascular coupling, is achieved through the integrated actions of neurons,

astrocytes, pericytes, and the endothelium (Girouard and Iadecola, 2006; Liu et al., 2013; Tian et al., 2010; Hall et al., 2014). Neurovascular coupling forms the basis of many neuroimaging methods, including blood oxygenation level-dependent (BOLD) functional magnetic resonance imaging (fMRI) and optical intrinsic imaging. Because functional imaging techniques detect changes in cerebral blood flow, volume, or oxygenation as surrogate markers of the underlying neural activity, understanding the mechanisms of neurovascular coupling is of vital interest to neuroscientists. Additionally, dysfunction of vascular response is common to many neurological disorders, substantiating its importance in maintaining a healthy brain (Girouard and Iadecola, 2006; Santisakultarm and Schaffer, 2011). Although many neurophysiological studies use anesthetic agents to maximize experimental control, anesthesia strongly influences brain physiology, including direct effects on vasotone, neurosuppresion, and alterations of inter-hemispheric activity (Liu et al., 2013; Shtoyerman et al., 2000). Therefore, understanding these cellular processes in the awake animal model is of great importance to neuroscience.

The lack of long-term optical imaging modalities in marmosets is a hurdle that prevents biomedical scientists from taking full advantage of this animal model. Optical imaging techniques such as two-photon microscopy (2PM) allow systematic, longitudinal investigation of neural activity and hemodynamics at the cellular level in awake, behaving animals (Chen et al., 2002; Ruiz et al., 2013). Despite the limitations of depth penetration compared to MRI-based methods, optical imaging tools are invaluable to capture both structural and functional information of multiple cells and cell types simultaneously with subcellular resolution in intact animals (Hall et al., 2014; Santisakultarm et al., 2012; Kleinfeld et al., 1998; Lecoq et al., 2011). The marmoset's lissencephalic cortex also ensures optical access to most functional areas of cortical tissue. Additionally, marmosets can be trained to rest comfortably with restraint, allowing researchers to bypass anesthesia and its confounding influences on brain physiology (Liu et al., 2013). Recently, 2PM was used to image neuronal populations in anesthetized marmosets (Sadakane et al., 2015). In the present study, we aim to establish a longitudinal two-photon imaging technique in awake marmosets, providing a critical tool to visualize cortical vasculature, neurons, and their dynamics at the cellular level.

2. Methods

2.1. Experimental overview

Three adult male marmosets were used in this study. All experiments were approved by the Animal Care and Use Committee of the National Institute of Neurological Disorders and Stroke. The timeline of experimental protocols began with acclimatization to body restraint and pre-operative testing of cognition and motor skills. Next, marmosets underwent surgical procedures for viral delivery of GCaMP and implantation of a head post and cranial chamber. Upon recovery, acclimatization to head restraint in the stereotaxic apparatus resumed along with post-operative testing of cognition and motor skills. Imaging experiments (*i.e.* awake and anesthetized 2PM) and continuous monitoring of post-operative cognition and motor skills followed in the subsequent months until euthanasia and immunohistochemistry of brain tissues.

2.2. Stereotaxic acclimatization

Animals were gradually accustomed to body restraint in the prone, sphinx position starting with 15 min of restraint on the first day of training and increasing by 15-min intervals up to 2 h at 3 times per week, over the course of 2 weeks (Silva et al., 2011). The behavioral assessment scale (Fig. S1) was used to monitor the marmoset's progress (Schultz-Darken et al., 2004). Similarly, animals were acclimatized to both body restraint and head-fixation in the custom-designed stereotaxic apparatus following implantation of the head post (Computer-aided design files available upon request; Figs. S2 and S3). The microscope stage (MP-285, Sutter Instrument) provides translation in X, Y, and Z, and the stereotax is secured to the stage by a mini lab jack (LJ750, Thorlabs) that provides additional course translation in Z. Angular positioning of the marmoset under the objective is obtained using a high precision ball & socket mounting platform articulating base (SL20, Thorlabs) that provides 360°of rotation.

2.3. Pre- and post-operative testing of cognition and motor skills

The Hill Staircase, the Valley Staircase, and the Six-Tube Search behavioral tasks (Marshall and Ridley, 2003) were administered biweekly before any surgical procedures were performed in order to evaluate any cognitive impacts of surgery, imaging, and longitudinal cranial chamber implantation. Briefly, animals were required to reach through vertical slots in a see-through screen panel to retrieve food rewards on each step of the staircase in the Hill and Valley Staircase tasks. Marmosets were given 3 min to obtain all rewards, and the cumulative score was recorded (score 1 for retrieving the reward on the nearest step, and 5 for the 5th farthest step). In the Six-Tube Search task, a food reward was hidden randomly in one of the six tubes. The marmoset was marked successful if it sought and obtained the treat within 30 s. If the retrieval was successful, the actual reach time was also recorded.

2.4. Viral delivery of GCaMP and cranial implantation

Animals were given dexamethasone and trimethoprim sulfa 1 day prior to surgery to minimize inflammation and infection (Table S2). During surgery, marmosets were intubated and mechanically ventilated at 35 breath/min (SAR-830/P, CWE) with 1.5–2% isoflurane anesthesia (Isoflurane Vaporizer, VetEquip) in 100% oxygen, and were maintained at 37.5°C with a rectal thermometer and a feedback-controlled heating pad (EW-12107-00, Cole-Parmer). The animals received an intravenous line in the tail vein for continuous saline (0.9% w/v) and drug administration before being placed in a stereotax (Model 900 with 1248 Adaptor, KOPF Instruments). Throughout the procedure, end-tidal CO_2, blood oxygen saturation, and heart rate were maintained within physiological ranges (SurgiVet® V9212AR, Smiths Medical). Using sterile techniques, a midline skin incision was performed to expose the skull so that lateral facial muscles could be scraped off of the bone, or resected as needed. Using stereotaxic coordinates, a 1-mm deep burr hole was hand drilled through the skull to provide injection access over Broadman Area 3b using a #7 drill bit (0.7-mm tip diameter; 19007-07, Fine Science Tools). Next, a micromanipulator (51950, Stoelting) with a 2-μL Hamilton syringe and a Neuros Adapter (32 gauge; 7002 KH SYR) were used to deliver 1 μL of the AAV1-hSyn-GCaMP5G viral construct (AV-1-PV2478, titer: 2.49×10^{13} genome copies/mL, Penn Vector Core). The needle was gradually lowered to 500 μm below

the cortical surface to infuse the virus at 0.1 μL/min (78-0311C, Cole-Parmer), assuming that the skull thickness was approximately 1 mm. After the intracranial injection, the needle was left in place for 10 min to allow diffusion into the surrounding tissue and to minimize backflow (Okada et al., 2013; Watakabe et al., 2015).

Once the syringe was slowly removed, 1 mL of Mannitol was administered intravenously to temporarily reduce brain volume to minimize the risk of increased intracranial pressure and cortical surface damage. A craniotomy was created using an electric drill (GX-7, Osseo Scientific) and a 10-mm circular drill bit (3/32" shank diamond core drill, Dad's Rock Shop) over the parietal cortex, encompassing the injection site. Our cranial chamber was designed using SolidWorks software (Dassault Systèmes SOLIDWORKS; file available upon request) and 3D printed (ProJet® 3510 HD, 3D Systems) with a biocompatible material (VisiJet® M3 Crystal, 3D Systems). The dura was carefully removed, and the chamber was placed over the craniotomy. We pre-install the cover glass on the cranial chamber so that the cortex would not be exposed to the air or dental cement (Ortho-Jet, Lang Dental) vapor. We then secured the cranial chamber flanges using dental cement, which were reinforced by bone screws that provided additional surface grooves for adhesion. One low-profile threaded polyether ether ketone (PEEK) headpost base was similarly adhered onto the medioposterior skull. The skull was then covered by dental cement to eliminate direct exposure. Finally, internal sutures were tied to hold facial muscles to the skin, and to reinforce the skin along the midline of the skull. The marmosets were allowed to recover on a heating pad before they were returned to their cages. In addition to continued dexamethasone and trimethoprim sulfa, marmosets were given meloxicam to minimize inflammation, infection, and discomfort in the subsequent 12 days of recovery (Table S1).

2.5. Two-photon microscopy and sensory stimulation

Two-photon imaging was performed with a commercial Zeiss LSM 780 NLO system (Carl Zeiss), pumped by a Chameleon Vision S (Coherent) with a motorized micromanipulator stage (MP-285, Sutter Instrument). Intravenous Texas Red-Dextran (TxRD; 0.4 mL of 2.5% w/v; D-1864, Invitrogen) and GCaMP were simultaneously excited at a 900-nm wavelength. Green and red fluorescence emission was relayed through bandpass filters, 525/50 and 635/40 nm (center wavelength/bandwidth), respectively. Low (5× air objective, NA = 0.25; FLUAR) and high-magnification (20× water immersion objective, NA = 1.0; W Plan-APOCHROMAT) images were acquired using Zen 2011 software (Carl Zeiss). Electrical stimulation to activate the median nerve was delivered through contact electrodes taped to the contralateral wrist at a frequency of 50 Hz at 0.5–2 mA with a 333 μs pulse width driven by a constant current stimulus adapter (STMISOC STM100C and MP150, BioPac) (Liu et al., 2013). For anesthetized imaging, the monkey was induced with 5% isoflurane and maintained at 1.5–2% in a 30:70, oxygen-medical air ratio (Low Flow Air/Oxygen Blender, Ohio Medical) via a facemask. While anesthetized, a heat pad was placed under the animal to preserve body temperature, and blood oxygen saturation and heart rate were maintained within physiological ranges.

2.6. Topological, structural, and hemodynamics analysis of cortical vasculature

Microvessels were manually traced from multiple adjacent 2PM image stacks aligned in three dimensions by maximizing the cross-correlation of fluorescence signal in the overlapping regions. Using a custom software package, vascular information such as vessel class, connectivity, and pathway were extracted. A single vessel segment was defined as the line path between two branch points. Penetrating arterioles and ascending venules were classified by both morphology and diameter (10 μm), leaving the remaining vessels classified as capillaries. The tortuosity (*i.e.* the "arc-chord ratio" or the actual vessel path length divided by the Euclidean distance from one end of the vessel to the other), capillary density, vessel length (defined as the length of the vessel between two branching points), depth, and capillary branch order from a penetrating arteriole (*i.e.* the first microvessels branching off of a penetrating arteriole is branch order 1, and the next microvessels branching off of branch order 1 vessels are classified as branch order 2, *etc.*) were determined using algorithms written in MATLAB software (Mathworks). Vessel density was calculated using vascular line path information and cortical tissue volume adjusted to account for the angle of the imaging focal plane and brain surface curvature in image stacks. Briefly, a plane was first linearly fitted to the surface of the tissue volume where pial vessels were located. The entire tissue sample was then rotated based on the calculated angle between the fitted plane and the actual plane of the brain surface so that the most shallow pial vessels in the tissue volume all start at the same depth of $z = 0$ μm. Following depth correction, vessel density of each stack data set was calculated column-by-column (*i.e.* X-Y of 50×50 μm) to account for uneven z-axis cortical depth visualized within each stack. Vessels that extended outside of these tissue columns were excluded. Branch order was determined by running multiple loops to assign first branch order to capillaries stemming from penetrating arterioles, followed by the subsequent connecting capillaries branches until the segments merged with ascending venules. Identification of stalled capillaries was performed as previously described (Santisakultarm et al., 2014). RBC flow speed and vascular diameter of arteriole, venule, and capillary vessels were measured using previously published methods (Hall et al., 2014; Santisakultarm et al., 2012) with minor modifications (Drew et al., 2011).

2.7. Analysis of stimulus-evoked neural activity

Motion in the XY imaging plane was corrected using TurboReg ImageJ plug-in (Thevenaz et al., 1998). Region of interest (ROIs) enclosing neuronal soma were manually selected. The normalized fluorescence change $(\frac{\Delta F}{F_0})$ was calculated over each epoch, where F_0 was taken to be the mean fluorescence during at least 2-s duration prior to the stimulus onset, and the F was the instantaneous fluorescence, averaged F_0 over the ROI, minus

Neurons that exhibited fluorescence change more than 8% to at least half of the 10 stimulus epochs were considered responsive (Chen et al., 2013). Their fluorescence was averaged across all 10 trials of stimulation, and temporally smoothed with a moving average filter (20%-of-samples wide) in order to measure time-to-peak and peak fluorescence change (Cianchetti et al., 2013).

2.8. Immunohistochemistry

Marmosets were deeply anesthetized and perfused intracardially with 4% paraformaldehyde in phosphate buffer. The brain was post-fixed and then cryoprotected with 30% sucrose at 4°C. Coronal sections of 40-μm-thickness encompassing the regions of interest were prepared from each hemisphere. For immunofluorescence, free-floating sections were blocked with blocking solution (10% normal donkey serum and 0.3% Triton X-100 in PBS, pH 7.4) for 1 h at room temperature, followed by overnight incubation with anti-neuronal nuclear protein (NeuN) antibody (1:1000; MAB377, EMD Millipore) and glial fibrillary acidic protein (GFAP) anti-body (1:1000; G3893, Sigma-Aldrich). The primary antibody was detected using donkey anti-mouse secondary antibody conjugated with Alexa Fluor® 546 (1:1000; A10036, Life Technologies) in combination with rabbit anti-green fluorescence protein (GFP) antibody conjugated with Alexa Fluor® 488 (1:1000; A21311, Life Technologies) for 2 h at room temperature. Nuclei were counterstained with 4′,6-Diamidino-2-phenylindole (DAPI; D9542, Sigma-Aldrich). Sections were visualized using a confocal microscope (LSM 780, Carl Zeiss).

2.9. Statistical analysis

Statistical analysis was performed using Prism (GraphPad) and MATLAB (Mathworks) software. D'Agostino-Pearson omnibus or Shapiro-Wilk normality tests were performed in all datasets to determine distribution shapes. For data sets that passed the normality test, we reported mean ± standard error of the mean, while median [interquartile range] was reported for the rest. Appropriate tests of comparison in specific experiments were performed and indicated in the results section.

3. Results

3.1. Custom-designed stereotaxic restraint and cranial chambers enabled 2PM in awake marmosets

High spatial-resolution brain imaging requires the subject to be absolutely still, with the cortical surface parallel to the objective's focal plane. To satisfy these requirements, we trained marmosets to be calm while in a stereotax during 2 h of imaging. Their acclimatization progress was continuously evaluated approximately every 2 weeks using the Non-human Primate Behavioral Assessment Scale (Table S2) to ensure minimal anxiety during experiments (Schultz-Darken et al., 2004). A stereotaxic device with multiple degrees of freedom (*i.e.* both rotatable and translatable) was specifically engineered to connect to the marmoset's headpost to provide additional stability during imaging (Fig. 1A and B). The cranial chamber was crafted to allow the 20× objective (W Plan-Apochromat, Carl Zeiss) to approach the surface of the optical window (Fig. 1C). Both the headpost and the cranial chamber were constructed to fit on the curved skull and included a removable cap to protect the cover glass when the animal was in the cage (Fig. S4). Throughout the duration of the study, the implantation site remained clean and infection-free (Fig. 2A).

3.2. Cranial chamber provided optical access to somatosensory cortex for 6 months

Throughout the 6-month duration of our study, pial and subsurface microvessels, as well as genetically encoded calcium indicator (GCaMP)-labeled neurons, were observed with 2PM. The pial vasculature was maintained throughout the experimental duration, with neomembrane formation and neovascularization between the cortical tissue and the cover glass appearing approximately 3 months after chamber placement (Fig. 2A). Consequently, the maximal obtainable visualization depth (as measured from the shallowest blood vessel to the deepest neural or vascular structure observed) decreased from 500 μm on day 9 after chamber implantation to approximately 150 μm 5 months later (Fig. 2B). This longitudinal optical access achieved detailed visualization of numerous cortical microvessels and neurons for 6 months (Fig. 2C and D).

3.3. Awake marmosets exhibited physiological hemodynamic responses and calcium transients

We virally transfected neurons with GCaMP to optically measure their activation. *Ex vivo* immunohistochemistry showed successful viral transduction in neurons within 1-mm radius from the injection site (Fig. 3A–C). *In vivo* baseline GCaMP expression remained observable throughout the 6 months of 2PM imaging. Additionally, vascular response at the single-vessel (post-operative day 156) and calcium transients at the single-cell level (post-operative days 57, 83, 92, and 140) in response to peripheral stimuli were observed in cortical layer II/III (Fig. 3D–F and Video S1). Up until day 83, 19% of GCaMP-labeled neurons (n = 42) on average were responsive to 10-s electrical stimulation of the contralateral wrist, with average peak fluorescence increase of $18.6 \pm 8.8\%$ at 7.6 ± 1.3 s following stimulation onset (Figs. S5 and S6). By day 140, only 5% of GCaMP-labeled neurons (n = 42) were responsive. This represent a significant deviation compared to the previous days ($p = 0.008$, Chi-square test). In contrast, 32% of arterioles (n = 22) in layer I–II/III were responsive with an average peak dilation of $13.8 \pm 3.7\%$ at 5.9 ± 0.8 s following the brief, 2-s peripheral stimulation on day 156 (Fig. S7). Following long, 30-s stimulation, arterioles did not exhibited significant change in diameter (n = 21, no significance, two-tailed Wilcoxon matched-pairs signed rank test). Additionally, neither capillaries (n = 81, no significance) nor venules (n = 24, no significance) showed vasotone changes following prolonged stimulation (Fig. S8).

3.4. Isoflurane anesthesia altered cerebral hemodynamics

To quantify differences in cerebrovascular physiology and neuronal activity under anesthesia, we performed experiments in both awake and anesthetized marmosets. When comparing the same cortical vessels, flow speed in pial arterioles was reduced by $24 \pm 8\%$ (n = 7, $p = 0.03$, two-tailed Wilcoxon matched-pairs signed rank test) with corresponding $16 \pm 5\%$ dilation ($p = 0.02$) in isoflurane-anesthetized state compared to while awake (Fig. 4A–C). In general, diameters of all classes of vessels significantly increased under this anesthesia (n = 121, $p < 0.0001$. For baseline values, see Fig. S9). The most prominent isoflurane-induced dilation was observed in smaller microvessels, leading to a capillary dilation of 10 [−0.9 to 28]%; n = 79, $p < 0.0001$. Conversely, arterioles and venules displayed smaller diameter increases (2.8 [−2.1 to 13]% and 5.1 [−5.3 to 13]%, respectively;

Fig. 4D and E). The fraction of stalled cortical capillaries (*i.e.* those showing no net movement of blood cells) increased from 2.4 [2–6.8]% in the awake state (n = 1077) to 11 [5.8–14]% under isoflurane (n = 592, *p* = 0.02, two-tailed Mann–Whitney test; Fig. 4F and G).

3.5. Marmosets exhibited vascular reorganization following long-term cranial implantation, but no cognitive deficit

Although the surgical implantation of the cranial chamber was minimally invasive, physiological changes over 6 months were observed. Histological evaluation of the cortex revealed some signs of astrocytic activation near the surgical site (Fig. 5A and B), but minimal gross changes in brain structure compared to the intact hemisphere and to control animals without any implants. To quantify vascular changes, we measured tortuosity (arc-length ratio), length, and density of arterioles, capillaries, and venules *in vivo* on brain hemispheres through the cranial chamber implant, and *ex vivo* on the intact hemispheres. In a control animal without cranial implants, only *ex vivo* measurements were available.

Cortical microvessels of marmosets exhibited large animal-to-animal variations in characteristics (Table 1). Hence, statistical comparisons of vascular structure were only performed on the hemispheres with and without cranial chamber of the same marmoset (Fig. 5C and D). Following the surgical procedures, notable vascular changes were found in penetrating arterioles and ascending venules (Fig. 5E and F). Penetrating arterioles on the chamber hemisphere had a 2.2 fold increase in tortuosity, compared to those on the no-chamber hemisphere (*p* = 0.03, Kruskal–Wallis multiple comparisons with Dunn's correction; Table 1). On the other hand, ascending venules on the chamber hemisphere branched twice as often as those on the no-chamber hemisphere (*p* = 0.02; Fig. 5G and Table 1). The length of capillaries on the chamber hemisphere of the brain was significantly shorter than those on the no-chamber hemisphere (*p* = 0.03; Table 1). Connectivity from a penetrating arteriole to an ascending venule was quantified to further investigate changes in the network topology. The median number of capillaries connecting a penetrating arteriole to an ascending venule was 8 (Liu et al., 2013; Tian et al., 2010; Hall et al., 2014; Santisakultarm and Schaffer, 2011; Shtoyerman et al., 2000) segments in both hemispheres (no significance, Kolmogorov–Smirnov test; Fig. 5H, Table 1, and Fig. S10). Capillary density was 51 and 55 cm of capillary length per mm^3 of cortical tissue for no-chamber and chamber hemispheres of the same marmoset, respectively (Table 1).

Despite the micro changes in the vasculature, we did not observe neurological deficits caused by the implant. The marmoset's motor skills and cognitive function were continuously monitored and assessed using Hill and Valley Staircase and Six-Tube Search Tasks (Marshall and Ridley, 2003). The purpose of the Hill and Valley Staircase tasks was to evaluate any changes in motor skills of the arms ipsilateral and contralateral to the cranial chamber implantation. The objective of the Six-Tube Search task was to detect spatial neglect. Prior to surgery, marmosets scored 10 (Shtoyerman et al., 2000; Chen et al., 2002; Ruiz et al., 2013; Santisakultarm et al., 2012; Kleinfeld et al., 1998; Lecoq et al., 2011) points (n = 9) for the left arm, and 10 [10–10] points (n = 11) for the right arm in both the Hill and Valley Staircase tasks. Compared to before surgeries, there was no significant

change in the behavioral scores for left (n = 21, no significance, Chi-square test) and right (n = 21, no significance) arms following subsequent surgical procedures and throughout the remaining experimental duration (Fig. 6A–D). On the Six-Tube search task, marmoset had a 91 ± 4.9% success rate (n = 18) in retrieving the rewards prior to surgeries, and 98 ± 1.3% afterwards (n = 60, no significance, two-tailed Mann-Whitney test; Fig. 6E). For successful retrievals, marmosets obtained the reward in 9.9 ± 0.6 s (n = 82) before implantation on average, and 7.6 ± 0.8 s (n = 291) afterwards (Fig. 6F). We found no statistical differences in search times between contralateral and ipsilateral tubes (n = 373, no significant difference, Multiple *t*-tests with 1% false discovery rate adjustment).

4. Discussion

We demonstrated a proof of principle for longitudinal visualization of neural activity and hemodynamics with single cell resolution in awake marmosets. This approach enabled 2PM of the cortical hemodynamics and neural activity for over 5 and 3 months, respectively, before optical quality deteriorated beyond perception. Marmosets acclimated to the stereotaxic apparatus with minimal anxiety, allowing for repeated image acquisitions over multiple hours. Importantly, preserved functional hyperemia and neural activity were measured under normal physiological conditions in the absence of confounds introduced by the use of anesthesia. In addition, we quantified the vasodilatory effects of isoflurane anesthesia on cerebral microvessels as well as the reduction in blood flow speed at the individual-vessel level. Although changes in brain physiology following the surgical procedures may have played a role in our results, the observed vascular reorganization was limited and was not accompanied by any observable alterations in the animal's motor skills or cognition.

Our results indicate that vasodilation as the result of neurovascular coupling can be measured longitudinally over more than 5 months in the somatosensory cortex of marmosets implanted with a long-term cranial chamber. On the contrary, detectable neural firing measured based on fluorescence change of GCaMP significantly decreased after 3 months of expression. We found that 32% of measured penetrating arterioles reached a peak dilation of approximately 14% at 6 s following a short stimulation onset. In our previous studies, the spatiotemporal evolution of functional hyperemia was measured using BOLD fMRI in awake marmosets (Silva et al., 2011). The hemodynamic response signal reached its peak value 4–5 s following the stimulus onset (Silva et al., 2011). In humans, BOLD fMRI times-to-peak are 5–7 s (Aguirre et al., 1998; Friston et al., 1995; Boynton et al., 1996), while in anesthetized rodents they can range from 2.5 to 5 s, depending on the imaging modality (Tian et al., 2010; Berwick et al., 2005; Martindale et al., 2003; Chen et al., 2009; Chen et al., 2011; Narayan et al., 1994; Sheth et al., 2005). This indicates that the cortical microvascular length in marmosets may be more similar to humans than to rodents, presenting an elongated dispersive contribution of the transit of deoxyhemoglobin through the post-capillary side of the cerebral vasculature. Functional hemodynamic changes measured in response to short stimuli from individual cerebral vessels in awake marmosets are in close agreement with previously reported values obtained in anesthetized rodents, in which 37–54% of arteriole branches responded to peripheral stimulation with an average dilation of 13–18% (Hall et al., 2014). On the other hand, long, continuous stimulation

produced no long-lasting vasodilation in arterioles, capillaries, and venules. This is in agreement with a previous report that the steady-state changes in blood volume were spatially localized only to the activated cortical column of the rat's whisker's barrel, unlike the initial transient neurovascular coupling response, which was spatially less specific (Berwick et al., 2008). In the present report we relied solely on stereotaxic coordinates to define the imaging area over primary somatosensory cortex, so it is possible that our imaging location was suboptimal with respect to the functional area of activation. In future work, it will be interesting to use diffuse optical intrinsic imaging techniques to mark the boundaries of the functional area of activation prior to imaging its center with 2PM.

The effects of isoflurane quantified in our study highlight the importance of careful investigation of normal and diseased brain mechanisms without anesthesia-induced confounds. In general, halogenated anesthetics enhance inhibitory postsynaptic activity while reducing excitatory synaptic activity (Campagna et al., 2003). Among other mechanisms, isoflurane specifically enhances $GABA_A$ (Gyulai et al., 2001) and strongly inhibits nicotinic acetylcholine receptors (Narahashi et al., 1998). Longitudinal exposure may impair learning and increase anxiety in subjects (Yonezaki et al., 2015). Further, neurovascular coupling in macaques was found to be compromised under isoflurane, showing reduced BOLD amplitudes and longer onset times (Li et al., 2014), along with significant alterations in the metabolic profile of the brain (Makaryus et al., 2011). Suppression of brain function likely contributed to these outcomes. However, isoflurane also directly affects the cardiovascular system. Specifically, reductions in mean arterial blood pressure, cardiac output, and heart rate, along with systemic vasodilation, lead to increased overall cerebral blood flow, adding to the departure from normal hemodynamic responses in the brain (Conzen and Peter, 1992). We found disproportional and much more prominent effects of isoflurane on capillaries and smaller arterioles than in large vessels, suggesting a very active role that these microvessels may play in cerebral blood flow regulation (Hall et al., 2014; Hutchinson et al., 2006; Stefanovic et al., 2008).

Although the GCaMP-labeled neurons in our experiments were responsive to peripheral stimulation of the wrist up to 3 months, their long-term expression could be improved by the use of transgenic technology, which would eliminate direct cytotoxicity from the injection injury and viral delivery overload. Efforts have been made to optimize injection procedures, but the animal-to-animal variability remains large (Watakabe et al., 2015). In the present study, 19% of GCaMP-labeled neurons were responsive to somatosensory stimulation in the first 3 months of experiments, compared to 20% in the mouse's visual cortex (Akerboom et al., 2012). However, soma morphology and fluorescence dynamics are notably altered in our study. Instead of a fast time-to-peak, fluorescence increased gradually during stimulation, reaching average peak intensity at 8.3 s following stimulation onset, perhaps due to long-term decline in cell health and decreased optical quality (Chen et al., 2013). It is essential to note that we did not attempt to examine the exact same neurons in multiple imaging sessions, and therefore different neurons from different cortical depths were sampled in imaging sessions carried out over the months of experiments. Because of the decreasing penetration depth with time, this could introduce sampling bias towards neurons that are more superficial as they are sampled more often than neurons that reside deeper in the cortex. To avoid such bias, we only examined the response from neurons residing in cortical

layer II, which were visible in all imaging sessions carried out over the time course of months.

Lastly, we evaluated the impacts of the necessary procedures to allow long-term optical access in the marmosets. Although we strive to preserve normal physiology as much as possible, we surgically removed a section of the skull and dura mater, which may have adverse effects on brain physiology. In the controls, microvascular structures were within ranges of previous studies in adult marmosets (average of 18–38 cm/mm^3 vessel length per cortical volume, 90.8 ± 4.8 μm segment lengths, 8.3–9.9 μm diameter (Risser et al., 2009)). However, below the optical chamber, the marmoset's cortex displayed alterations in microvascular structure, with increased penetrating arteriole tortuosity, frequent branching on the ascending venules, and shorter capillary segments as the most prominent changes following intracranial injection and chamber implantation. Likely, a combination of angiogenesis and vasculogenesis contributed to overall vessel reorganization at the micro level, similar to those observed in previous studies where brain injury and inflammation were present (Morgan et al., 2007) (as opposed to the pattern observed in development). In addition, glial activation and scar formation, similar to our results (Fig. 5B), was shown after a stab brain injury (Fawcett and Asher, 1999). However, we did not observe a significant change in vascular responsiveness despite microvasculature changes. In addition, behavioral assessment before and after surgical procedures and throughout the following 6-month study duration showed no deficit in dexterity, spatial awareness, and cognition. In contrast, a marmoset model of stroke displayed immediate and sustained contralateral neglect and spatial impairment (Marshall and Ridley, 2003; Cook et al., 2012). Therefore, our marmoset model exhibited microvascular reorganization, but displayed normal vascular responses and no cognitive deficits.

While we were able to efficiently control motion during most data collection, we still faced occasional challenges with vasomotion, respiration, and intracranial brain motion. Additionally, starting at day 99 following surgery, we observed growth of a highly vascularized neomembrane between the chamber glass and cortical tissue, similar to that encountered by other groups (Chen et al., 2002; Shih et al., 2012). Future work will include development of an artificial dura placed below or in place of the cover glass to limit neomembrane growth, reduce pulsatile brain motion, and allow for electrophysiological measurement, optogenetic manipulation, or pharmacological delivery to the cortical tissue during imaging (Ruiz et al., 2013; Sakas et al., 1990; Roe, 2007; Arieli et al., 2002). Our contribution will improve researchers' ability to investigate cellular processes in the cortex and subcortical structures of awake marmoset over time, provide insight on neurovascular coupling mechanisms, and provide a broad translational importance in the prevention and treatment of a wide range of neurological disorders.

In conclusion, these results demonstrate a proof of concept for the capability to perform longitudinal 2PM imaging of cerebral microcirculation and neuronal activity in awake marmosets. We have quantified the confounding effects of isoflurane anesthesia and the effects of long-term cranial implant on the brain physiology. This work provides a novel and insightful imaging technique to assess neurovascular coupling at the spatial resolution of the

neurovascular unit without anesthesia, allowing for investigation of critical mechanisms in many neurological disorders.

Supplementary Material

Refer to Web version on PubMed Central for supplementary material.

Acknowledgments

References

Aguirre GK, Zarahn E, D'Esposito M. The variability of human BOLD hemodynamic responses. Neuroimage. 1998; 8(4):360–369. [PubMed: 9811554]

Akerboom J, et al. Optimization of a GCaMP calcium indicator for neural activity imaging. J. Neurosci. 2012; 32(40):13819–13840. [PubMed: 23035093]

Arieli A, Grinvald A, Slovin H. Dural substitute for long-term imaging of cortical activity in behaving monkeys and its clinical implications. J. Neurosci. Methods. 2002; 114(2):119–133. [PubMed: 11856563]

Berwick J, et al. Neurovascular coupling investigated with two-dimensional optical imaging spectroscopy in rat whisker barrel cortex. Eur. J. Neurosci. 2005; 22(7):1655–1666. [PubMed: 16197506]

Berwick J, et al. Fine detail of neurovascular coupling revealed by spatiotemporal analysis of the hemodynamic response to single whisker stimulation in rat barrel cortex. J. Neurophysiol. 2008; 99(2):787–798. [PubMed: 18046008]

Boynton GM, et al. Linear systems analysis of functional magnetic resonance imaging in human V1. J. Neurosci. 1996; 16(13):4207–4221. [PubMed: 8753882]

Burman KJ, et al. Cortical and thalamic projections to cytoarchitectural areas 6Va and 8C of the marmoset monkey: connectionally distinct subdivisions of the lateral premotor cortex. J. Comp. Neurol. 2015; 523(8):1222–1247. [PubMed: 25556940]

Campagna JA, Miller KW, Forman SA. Mechanisms of actions of inhaled anesthetics. N. Engl. J. Med. 2003; 348(21):2110–2124. [PubMed: 12761368]

Chen LM, et al. A chamber and artificial dura method for long-term optical imaging in the monkey. J. Neurosci. Methods. 2002; 113(1):41–49. [PubMed: 11741720]

Chen Y, et al. Optical coherence tomography (OCT) reveals depth-resolved dynamics during functional brain activation. J. Neurosci. Methods. 2009; 178(1):162–173. [PubMed: 19121336]

Chen BR, et al. High-speed vascular dynamics of the hemodynamic response. Neuroimage. 2011; 54(2):1021–1030. [PubMed: 20858545]

Chen TW, et al. Ultrasensitive fluorescent proteins for imaging neuronal activity. Nature. 2013; 499(7458):295–300. [PubMed: 23868258]

Cianchetti FA, et al. Stimulus-evoked calcium transients in somatosensory cortex are temporarily inhibited by a nearby microhemorrhage. PLoS One. 2013; 8(5):e65663. [PubMed: 23724147]

Conzen P, Peter K. Pharmacodynamics of inhaled anaesthetics. Curr. Opin. Anesthesiol. 1992; 5(4):515.

Cook DJ, Teves L, Tymianski M. Treatment of stroke with a PSD-95 inhibitor in the gyrencephalic primate brain. Nature. 2012; 483(7388):213–217. [PubMed: 22388811]

Drew PJ, Shih AY, Kleinfeld D. Fluctuating and sensory-induced vasodynamics in rodent cortex extend arteriole capacity. Proc. Natl. Acad. Sci. U. S. A. 2011; 108(20):8473–8478. [PubMed: 21536897]

Fawcett JW, Asher RA. The glial scar and central nervous system repair. Brain Res. Bull. 1999; 49(6): 377–391. [PubMed: 10483914]

Friston KJ, et al. Analysis of fMRI time-series revisited. Neuroimage. 1995; 2(1):45–53. [PubMed: 9343589]

Girouard H, Iadecola C. Neurovascular coupling in the normal brain and in hypertension stroke, and Alzheimer disease. J. Appl. Physiol. 2006; 100(1):328–335. (1985). [PubMed: 16357086]

Gyulai FE, Mintun MA, Firestone LL. Dose-dependent enhancement of in vivo GABA(A)-benzodiazepine receptor binding by isoflurane. Anesthesiology. 2001; 95(3):585–593. [PubMed: 11575528]

Hall CN, et al. Capillary pericytes regulate cerebral blood flow in health and disease. Nature. 2014; 508(7494):55–60. [PubMed: 24670647]

Hung CC, et al. Functional mapping of face-selective regions in the extrastriate visual cortex of the marmoset. J. Neurosci. 2015; 35(3):1160–1172. [PubMed: 25609630]

Hutchinson EB, et al. Spatial flow-volume dissociation of the cerebral microcirculatory response to mild hypercapnia. Neuroimage. 2006; 32(2):520–530. [PubMed: 16713717]

Kleinfeld D, et al. Fluctuations and stimulus-induced changes in blood flow observed in individual capillaries in layers 2 through 4 of rat neocortex. Proc. Natl. Acad. Sci. U. S. A. 1998; 95(26): 15741–15746. [PubMed: 9861040]

Lecoq J, et al. Simultaneous two-photon imaging of oxygen and blood flow in deep cerebral vessels. Nat. Med. 2011; 17(7):293–898.

Li CX, et al. Effect of high dose isoflurane on cerebral blood flow in macaque monkeys. Magn. Reson. Imaging. 2014; 32(7):956–960. [PubMed: 24890304]

Liu JV, et al. fMRI in the awake marmoset: somatosensory-evoked responses, functional connectivity, and comparison with propofol anesthesia. Neuroimage. 2013; 78:186–195. [PubMed: 23571417]

Makaryus R, et al. The metabolomic profile during isoflurane anesthesia differs from propofol anesthesia in the live rodent brain. J. Cereb. Blood Flow Metab. 2011; 31(6):1432–1442. [PubMed: 21266982]

Mansfield K. Marmoset models commonly used in biomedical research. Comp. Med. 2003; 53(4): 383–392. [PubMed: 14524414]

Marshall JW, Ridley RM. Assessment of cognitive and motor deficits in a marmoset model of stroke. ILAR J. 2003; 44(2):153–160. [PubMed: 12652010]

Martindale J, et al. The hemodynamic impulse response to a single neural event. J. Cereb. Blood Flow Metab. 2003; 23(5):546–555. [PubMed: 12771569]

Morgan R, et al. Neovascularization following traumatic brain injury: possible evidence for both angiogenesis and vasculogenesis. Neurol. Res. 2007; 29(4):375–381. [PubMed: 17626733]

Narahashi T, et al. Ion channel modulation as the basis for general anesthesia. Toxicol. Lett. 1998; 100–101:185–191.

Narayan SM, Santori EM, Toga AW. Mapping functional activity in rodent cortex using optical intrinsic signals. Cereb. Cortex. 1994; 4(2):195–204. [PubMed: 8038568]

Okada H, et al. Robust long-term transduction of common marmoset neuromuscular tissue with rAAV1 and rAAV9, molecular therapy. Nucleic Acids. 2013; 2(5):e95. [PubMed: 23715217]

Risser L, et al. A 3D-investigation shows that angiogenesis in primate cerebral cortex mainly occurs at capillary level. Int. J. Dev. Neurosci. 2009; 27(2):185–196. [PubMed: 19038323]

Roe AW. Long-term optical imaging of intrinsic signals in anesthetized and awake monkeys. Appl. Opt. 2007; 46(10):1872–1880. [PubMed: 17356633]

Ruiz O, et al. Optogenetics through windows on the brain in the nonhuman primate. J. Neurophysiol. 2013; 110(6):1455–1467. [PubMed: 23761700]

Sadakane O, et al. Long-term two-photon calcium imaging of neuronal populations with subcellular resolution in adult non-human primates. Cell Rep. 2015; 13(9):1989–1999. [PubMed: 26655910]

Sakas DE, et al. Biologically inert synthetic dural substitutes. Appraisal of a medical-grade aliphatic polyurethane and a polysiloxane-carbonate block copolymer. J. Neurosurg. 1990; 73(6):936–941. [PubMed: 2230977]

Santisakultarm TP, Schaffer CB. Optically quantified cerebral blood flow. J. Cereb. Blood Flow Metab. 2011; 31(6):1337–1338. [PubMed: 21364601]

Santisakultarm TP, et al. In vivo two-photon excited fluorescence microscopy reveals cardiac- and respiration-dependent pulsatile blood flow in cortical blood vessels in mice. Am. J. Physiol. Heart Circ. Physiol. 2012; 302(7):H1367–H1377. [PubMed: 22268102]

Santisakultarm TP, et al. Stalled cerebral capillary blood flow in mouse models of essential thrombocythemia and polycythemia vera revealed by in vivo two-photon imaging. J. Thromb. Haemost. 2014; 12(12):2120–2130. [PubMed: 25263265]

Sasaki E, et al. Generation of transgenic non-human primates with germline transmission. Nature. 2009; 459(7246):523–527. [PubMed: 19478777]

Schultz-Darken NJ, et al. Novel restraint system for neuroendocrine studies of socially living common marmoset monkeys. Lab. Anim. 2004; 38(4):393–405. [PubMed: 15479554]

Sheth SA, et al. Spatiotemporal evolution of functional hemodynamic changes and their relationship to neuronal activity. J. Cereb. Blood Flow Metab. 2005; 25(7):830–841. [PubMed: 15744249]

Shih AY, et al. Two-photon microscopy as a tool to study blood flow and neurovascular coupling in the rodent brain. J. Cereb. Blood Flow Metab. 2012; 32(7):1277–1309. [PubMed: 22293983]

Shtoyerman E, et al. Long-term optical imaging and spectroscopy reveal mechanisms underlying the intrinsic signal and stability of cortical maps in V1 of behaving monkeys. J. Neurosci. 2000; 20(21):8111–8121. [PubMed: 11050133]

Silva AC, et al. Longitudinal functional magnetic resonance imaging in animal models. Methods Mol. Biol. 2011; 711:281–302. [PubMed: 21279608]

Stefanovic B, et al. Functional reactivity of cerebral capillaries. J. Cereb. Blood Flow Metab. 2008; 28(5):961–972. [PubMed: 18059431]

Thevenaz P, Ruttimann UE, Unser M. A pyramid approach to subpixel registration based on intensity. IEEE Trans. Image Process. 1998; 7(1):27–41. [PubMed: 18267377]

Tian P, et al. Cortical depth-specific microvascular dilation underlies laminar differences in blood oxygenation level-dependent functional MRI signal. Proc. Natl. Acad. Sci. U. S. A. 2010; 107(34):15246–15251. [PubMed: 20696904]

Watakabe A, et al. Comparative analyses of adeno-associated viral vector serotypes 1, 2, 5, 8 and 9 in marmoset, mouse and macaque cerebral cortex. Neurosci. Res. 2015; 93:144–157. [PubMed: 25240284]

Yonezaki K, et al. Postanesthetic effects of isoflurane on behavioral phenotypes of adult male C57BL/6J mice. PLoS One. 2015; 10(3):e0122118. [PubMed: 25806517]

HIGHLIGHTS

- Longitudinal 2-photon microscopy was performed in awake marmosets.

- Neurons were labeled with AAV-GCaMP to allow optical detection of neural activity.

- Neuronal and vascular responses to sensory stimulation were preserved for months.

- Vascular remodeling including increased tortuosity and branching was quantified.

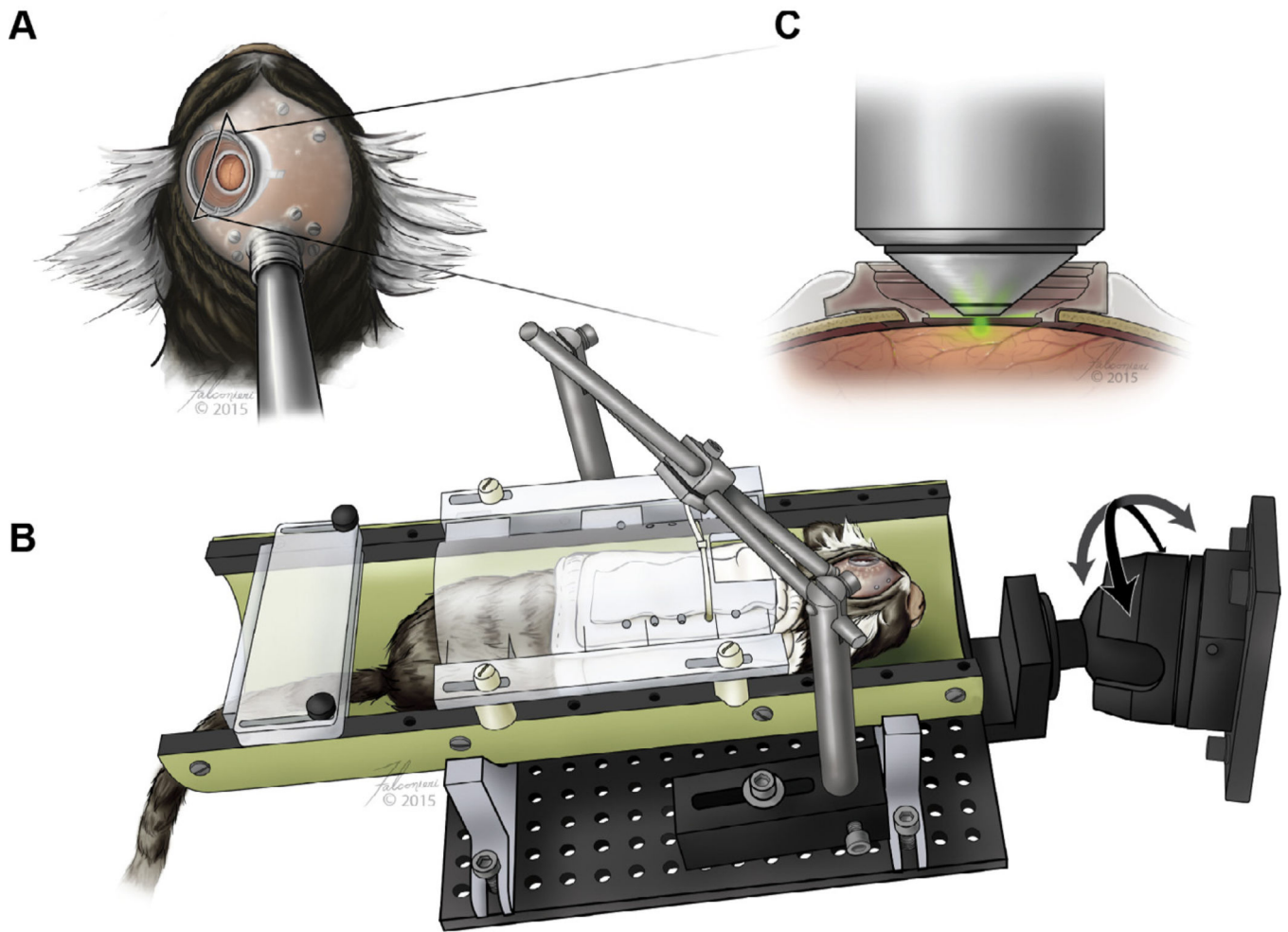- Isoflurane anesthesia modulated cerebral hemodynamics.

Fig. 1.
Design of cranial chamber and rotatable stereotaxic device. (A) Illustration of the relative locations of cranial chamber, supporting screws, and headpost on the marmoset. (B) Acclimated marmoset in a head-fixed rotatable stereotax that provides adequate stability and (C) 2PM optical access to image the brain.
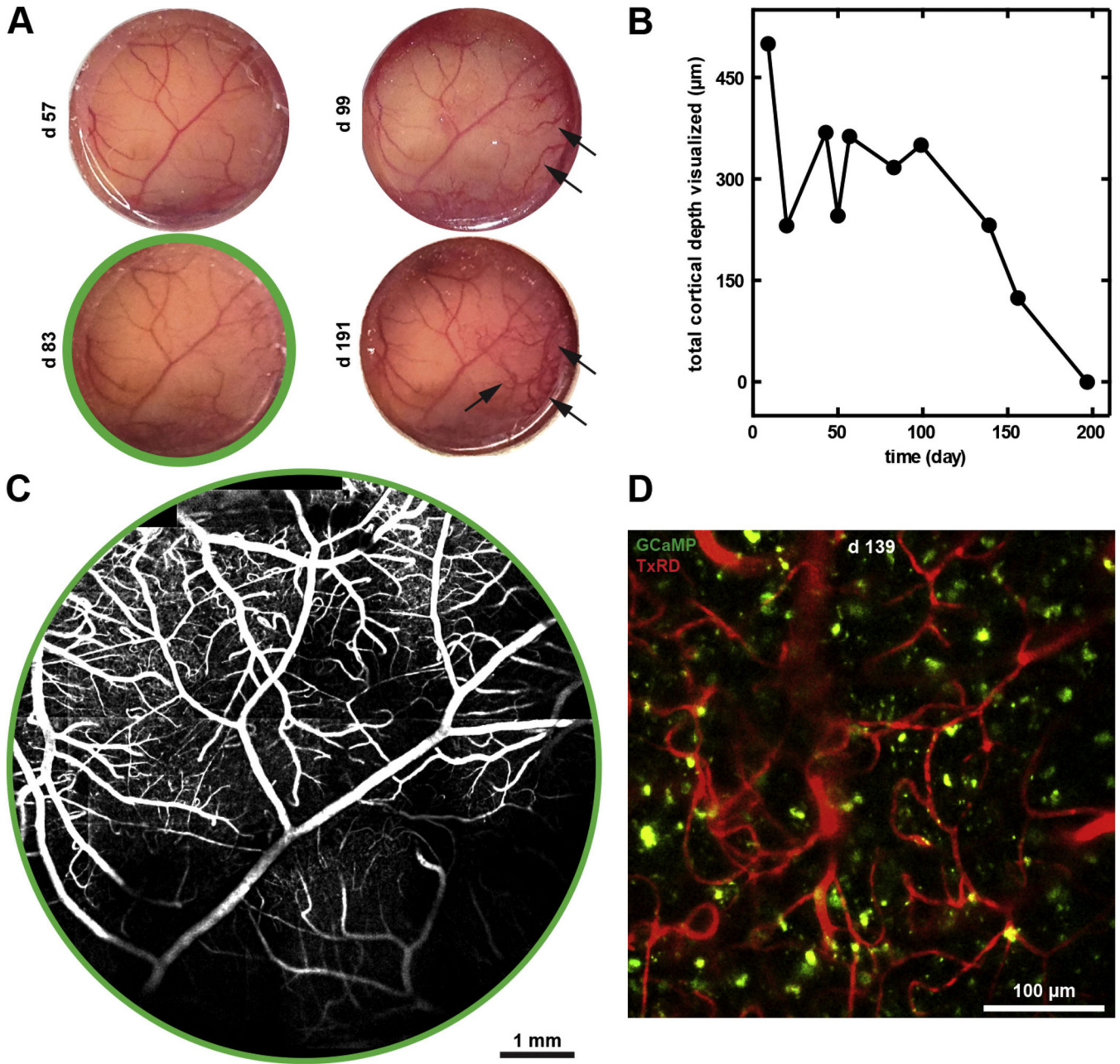
Fig. 2.
Cranial chamber implantation provided optical access to the cortex over 6 months. (A)
Sequential photographs of the cortex over 6 months following cranial implantation
demonstrated chamber stability, with neomembrane growth and vascularization (arrows)
after 3 months. (B) The total cortical depth visualized of marmoset C—measured from the
shallowest blood vessel to the deepest neural or vascular structure observed—deteriorated
from 500 μm over 200 days. (C) Low-magnification 2PM reconstructed images of surface
vasculature at 83 days after cranial chamber implantation. (D) High-magnification 2PM
image of vasculature (TxRD, red) and neurons (GCaMP, green) at 150 μm below the cortical
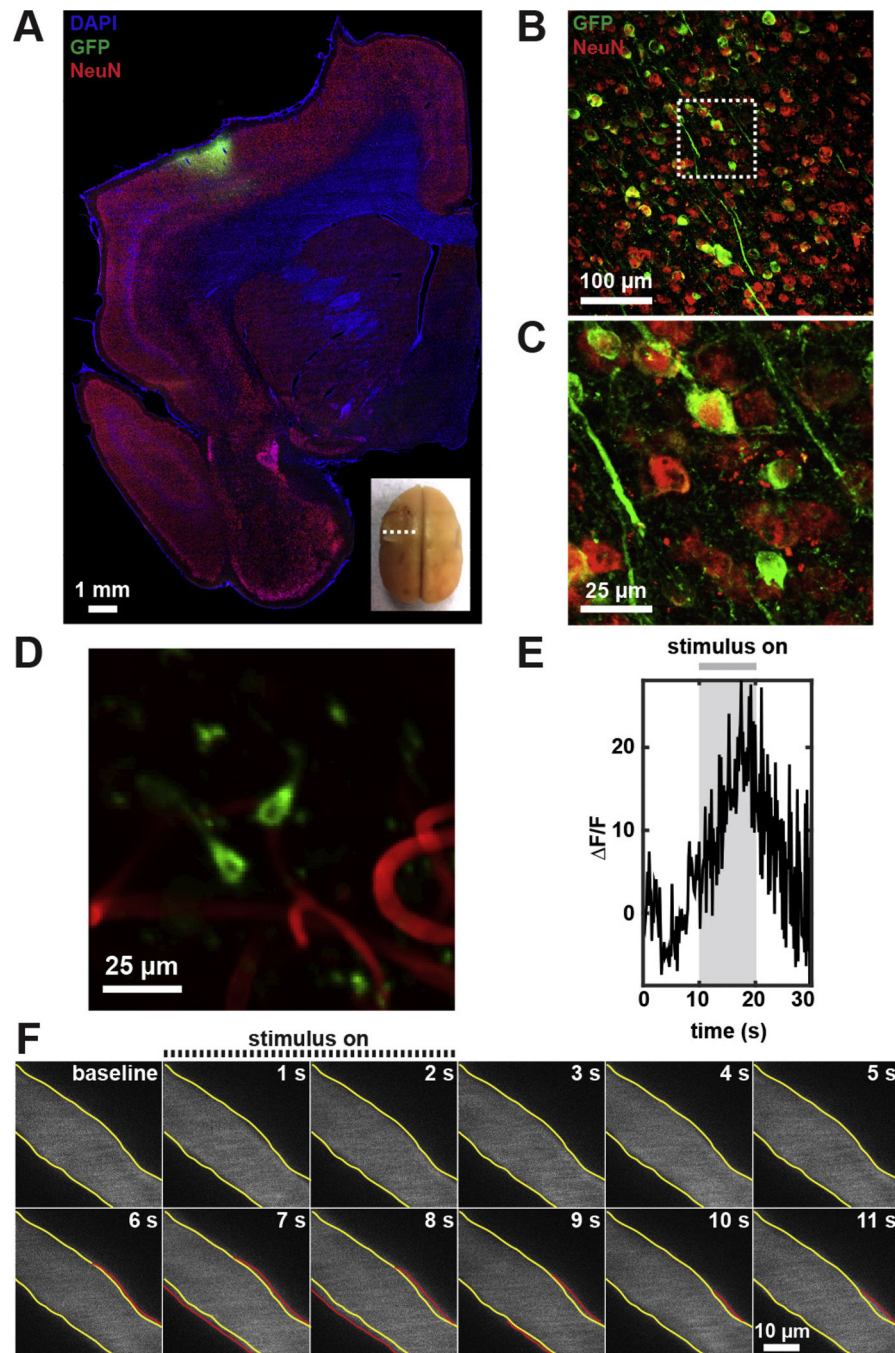surface at 139 days after chamber implantation.

Fig. 3.

Physiological vascular and neural response in awake marmosets. (A) Immunofluorescence staining of coronal brain section at the location indicated in inset. (B) Large numbers of GCaMP-expressing neurons (GFP, green) co-labeled with neuronal nuclear marker, NeuN (red), at 2 weeks following AAV1-hSyn-GCaMP5G intracranial delivery. (C) High-magnification confocal image of the boxed area in (B). (D) 2PM of a representative example of GCaMP-expressing neurons in layer II/III (240 μm below cortical surface) on day 57. (E) Average fluorescence change of responsive neurons (n = 9, from day 57–92), and (F) surface

arterial dilation following peripheral stimulation 156 days following cranial chamber implantation. The yellow contour identifies the baseline vessel diameter while the red contour indicates vasodilation following peripheral stimulation. The vasculature was labeled with intravenous administration of Texas Red-dextran.
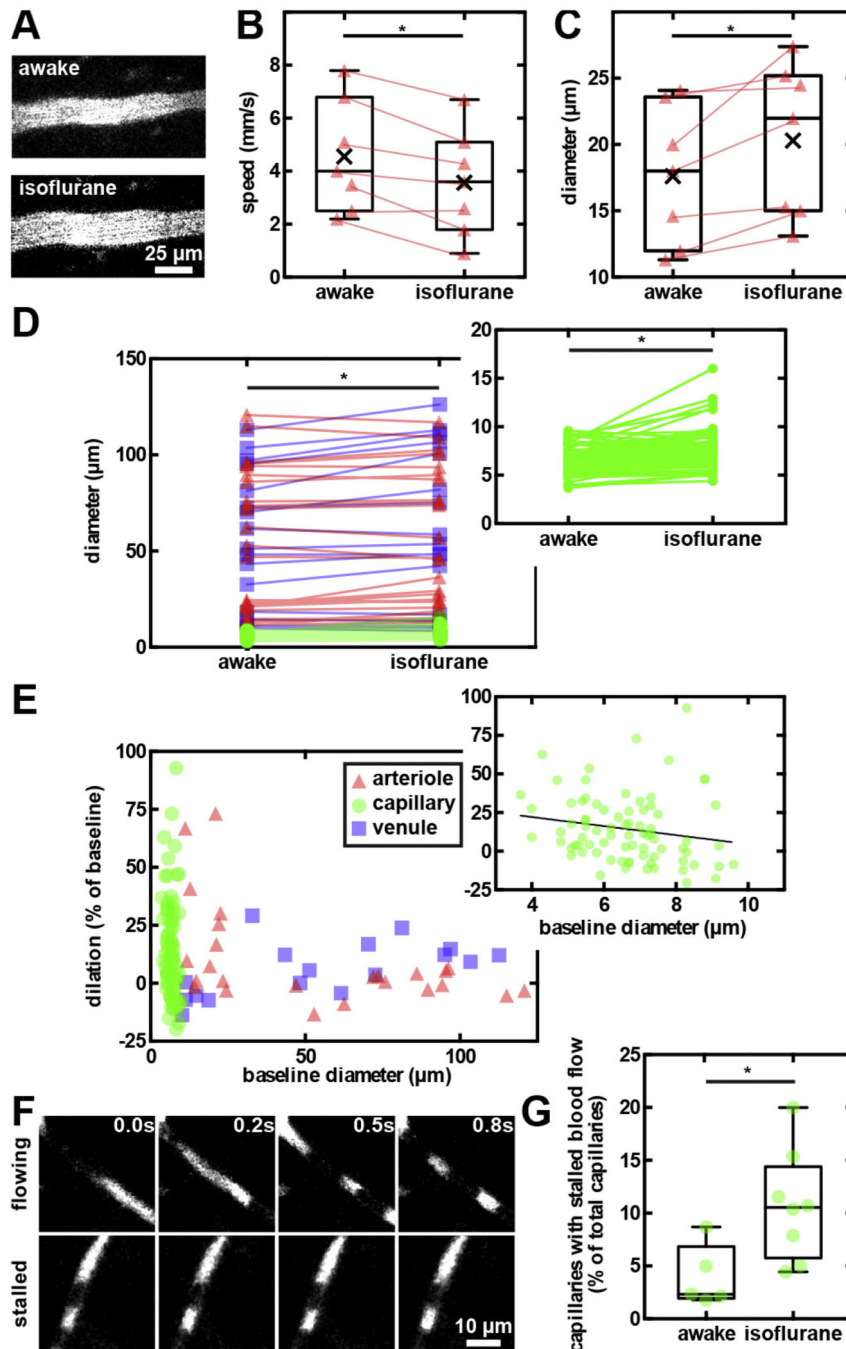
Fig. 4.
Effects of isoflurane on cerebral hemodynamics. (A) 2PM images of a small arteriole in awake and anesthetized marmoset. Box plots of decreased flow speed (B) and increased diameter (C) of paired cortical arterioles in awake and under isoflurane states. Connecting lines denote paired measurements of the same vessels. (D) Arterioles, capillaries (inset), and venules significantly dilated in isoflurane anesthetized marmosets compared to while awake. (E) The isoflurane-induced dilation is most prominent in capillaries and smaller arterioles. (F) Sequential 2PM images captured every 0.2 s that demonstrate flowing (top panels) and

stalled (bottom panels) capillaries in the cerebral cortex. Texas Red-dextran was intravenously injected to label blood plasma (bright), leaving the cellular components unlabeled (dark). (G) Box plots of the fraction of capillaries with stalled blood flow in awake and anesthetized animals.
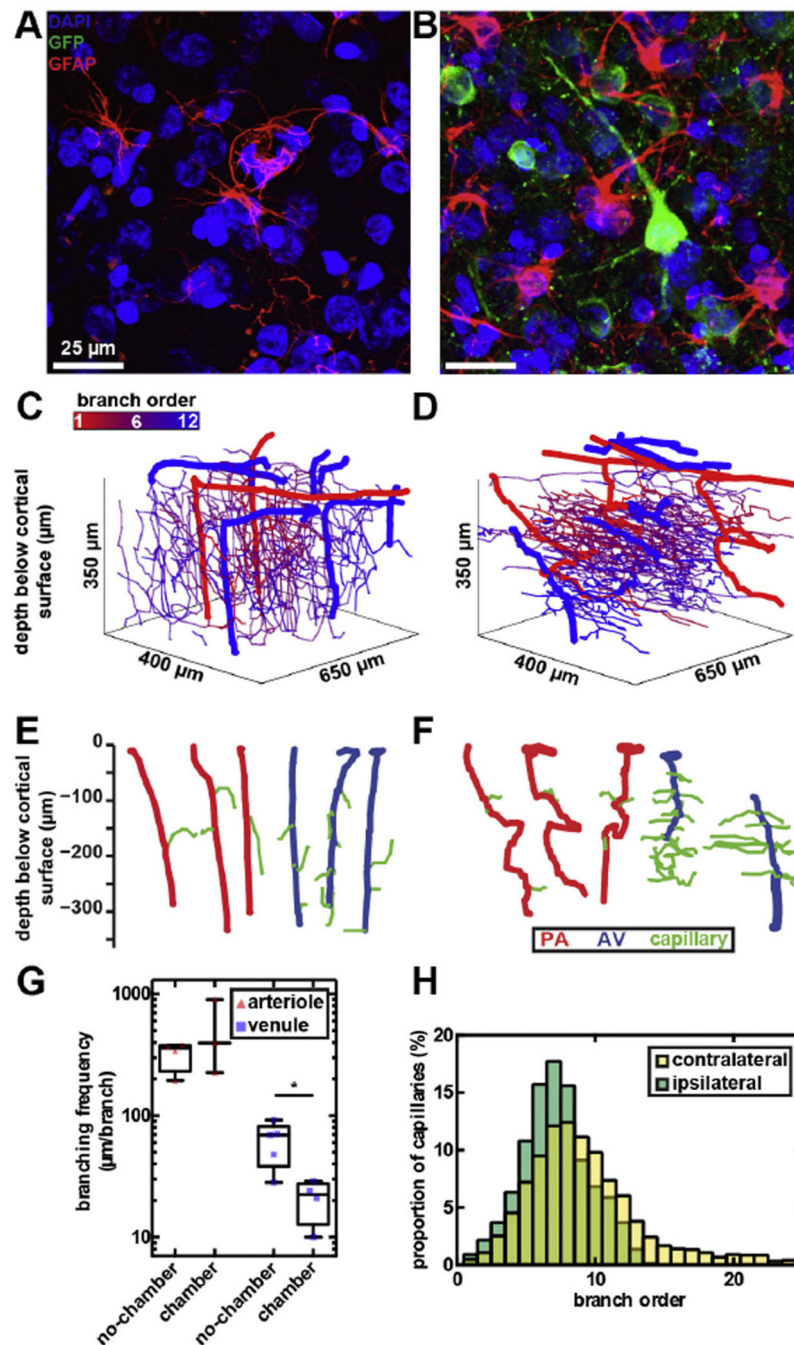
Fig. 5.

Vascular remodeling in marmosets with long-term cranial implants. Immunohistochemical staining of coronal brain sections from (A) no-chamber and (B) chamber hemispheres of the marmoset's cortex, 15 days post-operative showing astrocyte morphologies (GFAP, red), GCaMP-expressing neurons (GFP, green), and nuclei (DAPI, blue). Astrocytic soma and processes appeared enlarged with long-term implanted (B) compared the control hemispheres (A). (C and D) Cortical microvessel organization of (C) no-chamber and (D) chamber hemispheres of the marmosets 6 months after the implantation. Penetrating

arterioles and ascending venules in panels C and D were individually depicted in panels E and F. Penetrating arterioles and ascending venules from (E) no-chamber hemisphere were straight with infrequent branching into capillaries, compared to (F) those in the chamber hemisphere with increased tortuosity and (G) branching frequency. (H) Capillary connectivity from penetrating arterioles to ascending venules in the contralateral and ipsilateral sides was not significantly different.
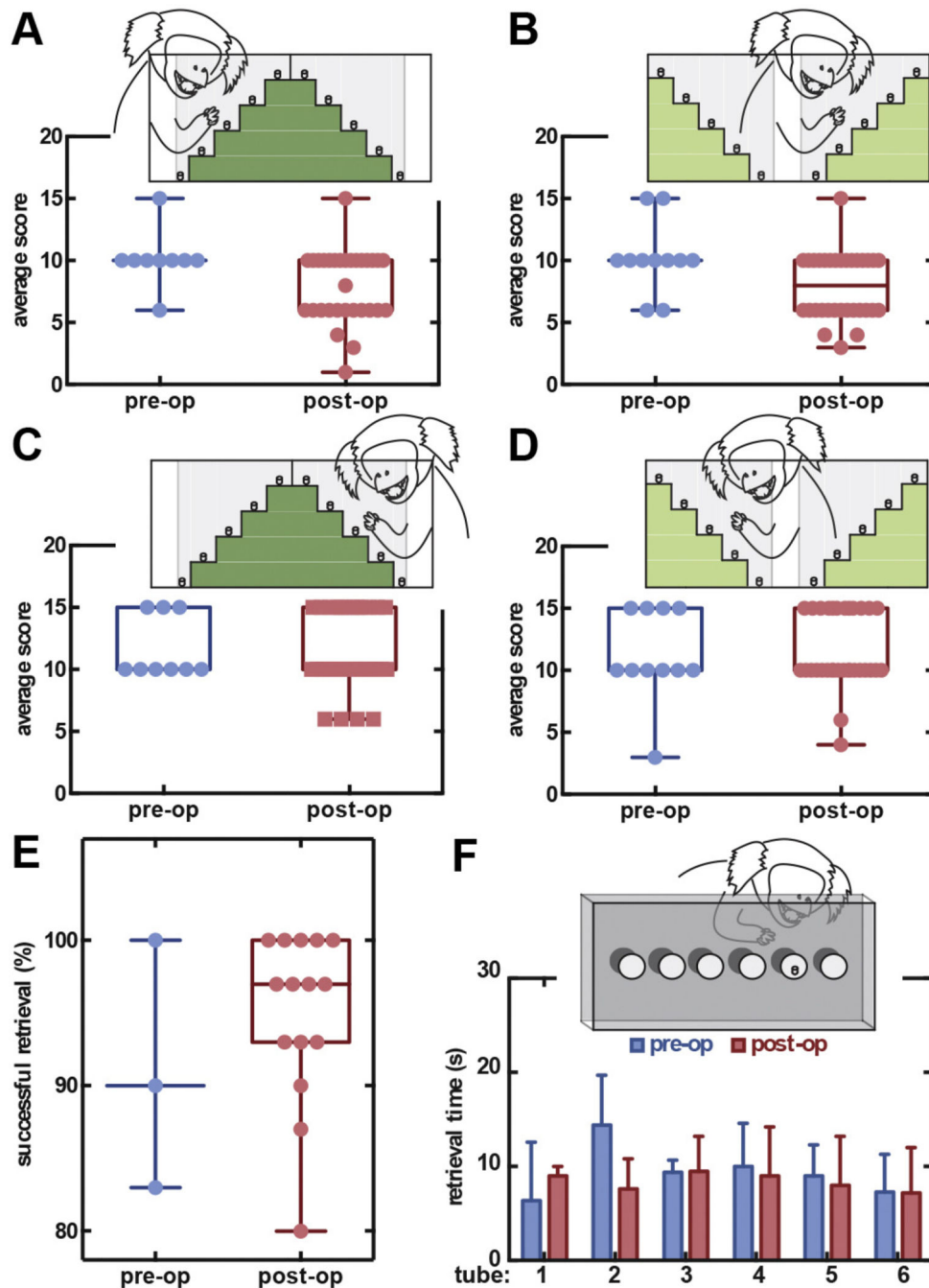
Fig. 6.

Behavioral assessments showed no cognitive and motor function impairment following long-term chamber implantation. Right-arm (A) Hill and (B) Valley Staircase and left-arm (C) Hill and (D) Valley Staircase tasks showed no change in scores before and after surgical procedures throughout the 6 months of experiments (each point represents 1 trial). The bottom and top of the boxes are show the first and third quartiles of the score. The band inside the box shows the median score. And the ends of the whiskers denote minimum and maximum of all scores. (E) Retrieval success in the Six-Tube Search task was not

statistically different with each point representing 1 trial (30 retrievals per 1 trial). (F) Retrieval time for both contralateral and ipsilateral tubes showed no spatial preference and neglect despite the cranial implantation.

Table 1

Vascular information of marmosets.

Subject	Tortuosity (arc-chord ratio)					Length (µm)			Branching (µm/branch)		PA-AV Connectivity (branch)	Vessel Density (cm/mm³)	
	Arteriole	PA	Capillary	Venule	AV	Arteriole	Capillary	Venule	PA	AV		All	Capillary
Marmoset B —control	1.0 [1.0–1.1]	1.4 [1.2–1.6]	1.2 [1.1–1.3]	1.1 [1.0–1.1]	1.2 [1.1–1.4]	173 [90–330]	81 [52–125]	86 [56–124]	350 [299–453]	39 [29–88]	7 [6–9]	42	37
Marmoset C—no-chamber hemisphere	1.0 [1.0–1.1]	1.3 [1.2–1.5]	1.2 [1.1–1.3]	1.1 [1.0–1.1]	1.1 [1.1–1.6]	176 [113–233]	74 [47–116]	83 [54–115]	358 [232–381]	70 [38–82]	8.5 [6–10]	63	55
Marmoset C—chamber hemisphere	1.3 [1.0–2.3]	2.9 [2.5–3.7]	1.2 [1.1–1.4]	1.1 [1.0–1.1]	2.9 [1.1–4.5]	202 [149–430]	70 [42–109]	66 [36–117]	396 [227–902]	23 [13–28]	8 [7–10]	57	51
Marmoset S—chamber hemisphere	1.0 [1.0–1.0]	–	1.1 [1.1–1.2]	1.1 [1.1–1.2]	–	114	80 [56–116]	69 [41–89]	–	–	8 [7–9]	42	39

Data were reported as median [interquartile range].

PA—Penetrating arteriole; AV— Ascending venule.

Branching was reported as µm of vessel length per each branching.

Number of capillary branches between PA and AV was used to quantify connectivity.

Vessel density was reported as vessel length/cortical volume.